

## Obscured clusters.

### III. Follow-up observations of Mercer 23<sup>\*</sup>

M. M. Hanson<sup>1</sup>, R. Kurtev<sup>2</sup>, J. Borissova<sup>2</sup>, L. Georgiev<sup>3</sup>, V. D. Ivanov<sup>4</sup>, D. J. Hillier<sup>5</sup>, and D. Minniti<sup>6</sup>

<sup>1</sup> Department of Physics, University of Cincinnati, Cincinnati, OH 45221-0011, USA  
e-mail: margaret.hanson@uc.edu

<sup>2</sup> Departamento de Física y Astronomía, Facultad de Ciencias, Universidad de Valparaíso, Av. Gran Bretaña 1111, Playa Ancha, Casilla 5030, Valparaíso, Chile  
e-mail: [radostin.kurtev; jura.borissova]@uv.cl

<sup>3</sup> Instituto de Astronomía, Universidad Nacional Autónoma de México, Apartado Postal 70-254, CD Universitaria, CP 04510 Mexico DF, Mexico  
e-mail: georgiev@astro.unam.mx

<sup>4</sup> European Southern Observatory, Ave. Alonso de Cordova 3107, Casilla 19, Santiago 19001, Chile  
e-mail: vivanov@eso.org

<sup>5</sup> Department of Physics and Astronomy, University of Pittsburgh, Pittsburgh, PA 15260, USA  
e-mail: Hillier@pitt.edu

<sup>6</sup> Departamento de Astronomía y Astrofísica, Pontificia Universidad Católica de Chile, Avenida Vicuña Mackenna 4860, 782-0436 Macul, Santiago, Chile and Vatican Observatory, V00120 Vatican City State, Italy  
e-mail: dante@astro.puc.cl

Received 15 August 2009 / Accepted 13 April 2010

#### ABSTRACT

**Context.** New infrared surveys have revealed over 1000 new open cluster candidates in the Milky Way, but these candidates need to be confirmed with follow up observations. Of particular interest are young, massive star clusters because they serve as nearby analogues to the distant super star clusters studied as point sources in other galaxies.

**Aims.** We determine the physical parameters and investigate the high-mass stellar content of the infrared star cluster Mercer 23, situated near the Galactic plane ( $l = 53^{\circ}772$ ,  $b = +0^{\circ}164$ ).

**Methods.** Our analysis is based on new Baade/PANIC  $JHK_S$  and ISAAC/VLT imaging of Mercer 23 and ISAAC/VLT moderate resolution ( $R \approx 4000$ ) spectroscopy of the brightest cluster members in the  $H$ - and  $K$ -bands. The cluster age is determined from isochrone main-sequence (MS) and pre-MS fitting. We derive stellar parameters for eight of the stellar members, using a full non-LTE modeling of the obtained spectra.

**Results.** Mercer 23 is a very young cluster, with age of  $t = 2-4$  Myr. The cluster suffers reddening of  $E(J-K_S) = 1.35$ ,  $A_V = 7.2$  mag. The derived distance is  $d = 6.5 \pm 0.3$  kpc. Our spectral modeling allows us to conclude that the three most luminous member are evolved highly massive stars: a WR star, and two mid-O supergiant stars, based on their derived luminosity.

**Conclusions.** Mercer 23 is not a super-massive cluster such as those recently recognized to exist in the Milky Way. However, its mass estimate of  $4-6 \times 10^3 M_{\odot}$  and possibly more, puts it in the class of young Galactic clusters hosting WR stars.

**Key words.** Galaxy: open clusters and associations: general – stars: Wolf-Rayet – open clusters and associations: individual: [MCM2005b] 23

## 1. Introduction

The study of massive Milky Way star clusters has been propelled to a new level of urgency with the recent recognition that Westerlund 1, known to Galactic astronomers for almost 50 years, has a mass in the range of extragalactic super star clusters (SSCs). SSCs have been of great interest and considerable study by extragalactic astronomers since their discovery some 15 or more years ago (Holtzman et al. 1992). Critical questions about the cluster mass function (CMF), cluster disruption times, and whether there exists a global or locally dependent upper mass limit for stellar clusters, are central to the current debates of astronomers studying extragalactic stellar clusters (Gieles 2009).

By it's new association to SSCs, these same critical questions now extend to studies of our Milky Way stellar clusters.

Despite their distance, the CMF within other galaxies is considerably easier to derive than in our local Milky Way because the entire galaxy (when mostly face on) is clearly in view. To be sure, biases exist in the interpretation of extragalactic observations, but selection effects like those endured by researchers searching our own Milky Way seem negligible by comparison. Yet, how do the numbers look presently in the Milky Way and does it fit into the scenario laid out by extragalactic astronomers studying stellar clusters in distant spirals? New, deep, infrared surveys (2 MASS, DENIS, GLIMPSE, ongoing VISTA-VVV Survey, Minniti et al. 2010) provide great promise in reducing the selection effects which plagued decades of optical surveys in the Milky Way. Following the release of these surveys, a cottage industry has blossomed in the identification of new, candidate Milky Way star clusters (Dutra & Bica 2000; Dutra et al. 2003; Bica et al. 2003; Mercer et al. 2005; Froebrich et al. 2007).

<sup>\*</sup> Based on observations gathered with the New Technology Telescope and ISAAC, VLT of the ESO within observing programs 77.D-0089 and 81.D-0471 and the 6.5 m Magellan Telescopes located at Las Campanas Observatory, Chile.

Several years ago we embarked on a long-term project to observe candidate star clusters in the inner Milky Way and to study them in much greater detail (Borissova et al. 2003, 2005, 2006, 2008; Ivanov et al. 2002, 2005; Kurtev et al. 2007, 2008, 2009; Hanson et al. 2008). Initially, this project was based on cluster candidates located with the 2MASS mission (Skrutskie et al. 2006), taking advantage of the reduced extinction in the near-IR. However, recent advances in mid-IR instrumentation have made it possible to carry out all-sky IR surveys in this spectral region, too. The recent *Spitzer Space Telescope* Galactic Legacy Infrared Mid-Plane Survey Extraordinaire (GLIMPSE, Benjamin et al. 2003) offers an excellent opportunity to carry out an even deeper census of such objects than was possible with 2MASS. GLIMPSE is an excellent tool for finding obscured clusters in the Galactic disk because the extinction in the mid-IR is a factor of 2–5 lower than in the near-IR.

Recently, Mercer et al. (2005) carried out a comprehensive search for clusters in the mid-IR using the point source catalog of GLIMPSE. They reported 92 cluster candidates worthy of follow up study. In this study, we continue the investigation of one of these candidate Mercer clusters, [MCM2005b] 23 (hereafter Mercer 23). Other identifiers of this cluster are DSH J1930.2+1832 and Teutsch 42 Kronberger et al. (2006). They determined the reddening, distance and age of the cluster using 2MASS photometry and solar metallicity Padova isochrones. Kronberger et al. (2006) determined the visual diameter of the cluster of 1.2 arcmin,  $E(B-V)=2.55$ , distance to the cluster 1.6 Kpc and age of 32 Myr. They also pointed out the presence of the X-ray source 2E 1928.0+1825 = 2RXP J193013.8+183216 (Harris et al. 1994) located very close to the cluster center at the distance of  $12 \pm 10$  arcsec (ROSAT 2000).

In this paper, we report our first results for Mercer 23 (Fig. 1) – a compact young cluster located near the Galactic plane ( $l = 53^\circ 772$ ,  $b = +0^\circ 164$ ) containing at least two very massive, evolved members, and one WR star. The cluster membership provides observational constraints upon the age and initial mass of short-lived evolved, massive stars. In this paper we present the main results of our near-IR photometric and mid-resolution spectral analysis of the cluster stars and its newly discovered WR star.

## 2. Observations and data reduction

### 2.1. Photometry

Broadband  $JHK_S$  imaging of Mercer 23 was carried out with the near-IR imager PANIC (Martini et al. 2004) at the 6.5-m Baade telescope at the Las Campanas Observatory and with the ALADDIN detector of the ISAAC, VLT, ESO. The PANIC instrument uses a  $1024 \times 1024$  HgCdTe Hawaii detector array; the scale is  $0.125$  arcsec pixel $^{-1}$  giving a total field of view of  $2.1 \times 2.1$  arcmin. The ALADDIN array has pixel scale of  $0.1478$  arcsec pixel $^{-1}$  and the maximum field of view is  $151 \times 151$  arcsec. All observations are made in jittering mode with 20 arcsec jitter box size under moderate atmospheric conditions (seeing 0.8–1.2 arcsec). The observing log is given in Table 1, and three-color composite images of Mercer 23 are shown in Fig. 1.

The images are reduced following the “standard” procedures for the infrared, which include flat-fielding, sky subtraction, alignment and combination into a final image. The photometry was obtained using the DAOPHOT package within the Image Reduction and Analysis Facility (IRAF)<sup>1</sup>. All observing runs

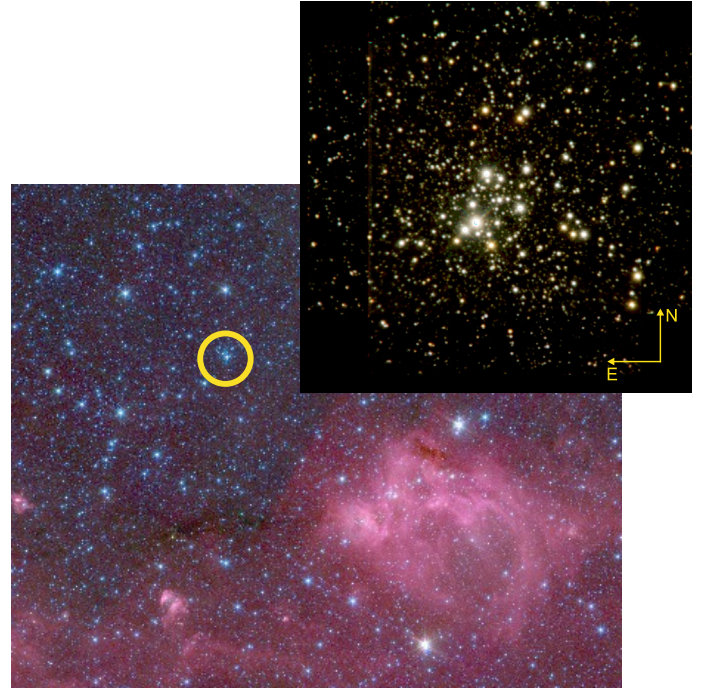


**Fig. 1.** Lower left, the GLIMPSE *Spitzer Space Telescope* true color image of the region around Mercer 23 from [3.6], [4.5], [5.8] bands. Upper right, the true color composite image from  $JHK$  PANIC frames covers approximately  $2 \times 2$  arcmin is presented on the upper right corner. This image is centered at the cluster with coordinates:  $\alpha(2000) = 19^{\text{h}} 30^{\text{m}} 13^{\text{s}}.5$  and  $\delta(2000) = 18^\circ 32' 10''$ . North is up and East is to the left.

**Table 1.** The log of observations of Mercer 23.

Instr.	Filter	Min DIT	Exp. Time	Date
		s	s	
Panic	$J$	3	93	14.07.2006
	$H$	3	93	14.07.2006
	$K_S$	3	90	14.07.2006
Panic	$J$	10	300	14.07.2006
	$H$	10	300	14.07.2006
	$K_S$	10	300	14.07.2006
ISAAC	$J$	0.5	9	13.06.2008
	$H$	0.5	9	13.06.2008
	$K_S$	0.5	9	13.06.2008

(obtained with the PANIC and ALADDIN imagers) were reduced independently. The typical photometric errors vary from 0.01 mag for stars with  $K_S \sim 10$  mag to 0.10 mag for  $K_S \sim 18$  mag and 0.15 mag for  $K_S \sim 19$  mag. The photometric calibration was performed by comparing our instrumental magnitudes with the 2MASS measurements of about 1330 stars, covering the color range  $0.0 \leq J-K_S \leq 3.0$  mag and magnitude range  $10 \leq K_S \leq 14.5$  mag. A least squares fit of the instrumental PANIC  $jhk$  magnitudes to the standard 2MASS system gave the following relations:

$$(J - K_S) - (j - k_S) = 0.587_{(\pm 0.008)}$$

$$J - j = 0.007_{(\pm 0.010)} \times (J - K_S) + 0.719_{(\pm 0.012)}$$

$$H - h = -0.023_{(\pm 0.011)} \times (J - K_S) + 0.292_{(\pm 0.009)}$$

$$K_S - k_S = -0.005_{(\pm 0.009)} \times (J - K_S) - 0.132_{(\pm 0.004)}.$$

<sup>1</sup> IRAF is distributed by the National Optical Astronomy Observatories, which are operated by the Association of Universities

for Research in Astronomy, Inc., under cooperative agreement with the National Science Foundation.

**Table 2.** Positional and photometric data for spectroscopically observed stars in Mercer 23.

Object	RA(J2000) deg	Dec(J2000) deg	$J$ mag	Err $J$ mag	$H$ mag	Err $H$ mag	$K_S$ mag	Err $K_S$ mag	Magnitude Source	Spectral type	RV km s <sup>-1</sup>	Err RV
Obj1*	292.557583	18.533426	10.615	0.033	9.834	0.032	9.524	0.041	2MASS	O5.5I	–	–
Obj2	292.556499	18.534004	8.646	0.021	7.835	0.017	7.332	0.020	2MASS	WR	–	–
Obj3	292.553464	18.536149	13.853	0.021	13.062	0.019	12.700	0.021	PANIC	O9/B2	86	2
Obj4	292.547841	18.539963	13.168	0.025	12.382	0.020	12.019	0.020	PANIC	O9/B2	67	4
Obj5	292.556914	18.539985	15.379	0.020	14.478	0.021	14.117	0.019	PANIC	B	88	10
Obj6	292.555502	18.538446	10.199	0.026	9.420	0.029	9.033	0.024	2MASS	O6If	–	–
Obj7	292.554421	18.537366	14.688	0.021	13.834	0.021	13.452	0.022	PANIC	B	83	11
Obj8	292.552262	18.535301	10.875	0.025	10.126	0.027	9.861	0.022	2MASS	field	–	–
Obj9	292.553299	18.532497	13.932	0.023	13.063	0.022	12.700	0.020	PANIC	O9/B2	67	12
Obj10	292.552102	18.531113	13.193	0.021	12.338	0.019	11.975	0.020	PANIC	O9/B2	80	8
Obj11	292.554488	18.533974	13.043	0.019	12.223	0.019	11.854	0.020	PANIC	O9/B2	91	9

**Notes.** The magnitudes of the brightest stars, saturated on PANIC images, are taken from 2MASS. The magnitudes of Obj1, noted with asterisk, are obtained by us from PSF photometry on 2MASS images.

Similar equations and errors are obtained for the ALADDIN images. The final common list contains equatorial coordinates and  $JHK_S$  magnitudes of 3280 stars with photometric errors less than 0.15 mag. Artificial star tests show that the 80% completeness limit of the photometry is at  $J = 19.1$  and  $K_S = 17.4$  mag. The final errors are calculated, taking into account the photometric errors, errors from the transformation to the standard system and the standard deviation from the mean magnitude in the case of common stars in PANIC and ALADDIN photometry. They are given in Table 2.

## 2.2. Spectroscopy

On 14 July 2008, we obtained spectra at the 8.2-m Unit 1 telescope of the ESO Very Large Telescope (VLT), located on Cerro Paranal in Atacama, Chile, with the Infrared Spectrometer Array Camera (ISAAC, Moorwood et al. 1998). ISAAC employs a Rockwell Hawaii 1024 × 1024 array. The pixel scale of the detector is 0.146 arcsec pixel<sup>-1</sup>. Our spectra were obtained with the slit width of 0'.6, giving a spectral resolution of approximately 4000 (slightly more in the  $K$ -band, and slightly less in the  $H$ -band). The grating was centered at two positions, 1.705 and 2.150  $\mu\text{m}$  in the  $H$ - and  $K$ -band, respectively. During the observations the seeing was good to very good, typically below 0'.7 and at times as low as 0'.5, though cirrus clouds came and went through the night.

In order to provide background subtraction, our observing strategy involved obtaining two main offset positions, A and B, on the cluster with an additional 5'' dither within the offset position for further unique positioning. We obtained spectra using three unique slit positions on the cluster. Each of the three slit positions yielded from 3 to 5 stars for which the signal was high enough to extract a spectrum. Regrettably, we ran out of time to obtain an  $H$ -band spectrum for one slit setting, leaving us without  $H$ -band spectra for Objects 5, 6, 7 and 8.

For the spectroscopic reduction, we used a combination of IRAF and the ESO *eclipse* package (Devillard 2001) while following the ISAAC Data Reduction Guide (Version 1.5, dated January 30, 2002). Salient steps in the reduction include: correction of ghost images on the array, subtracting off source positions from on source positions, dividing by the flat field, removing the spectral warp in the two dimensional images, then extracting and integrating the individual two-dimensional spectra.

Wavelength calibration was achieved using Xenon and Argon arc-lamps obtained during the night and daytime

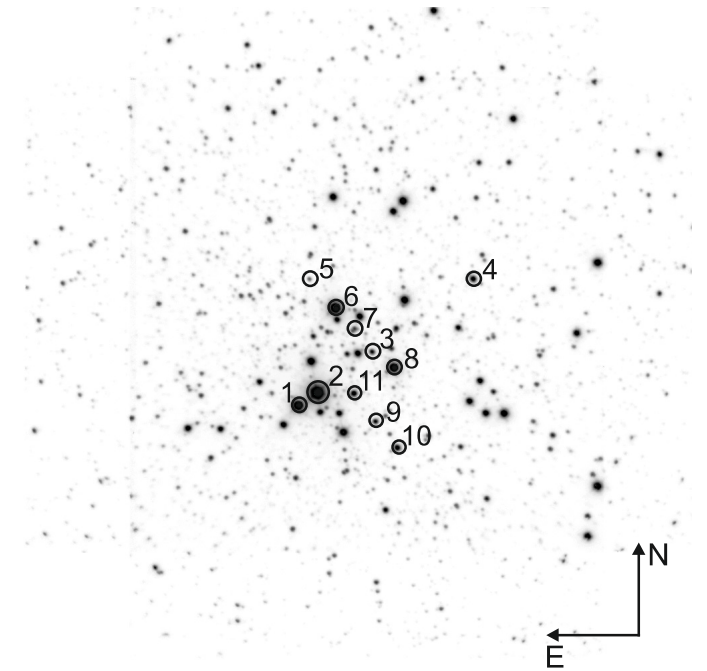


**Fig. 2.** Identification of the stars with near-IR spectroscopy listed in Table 2. The field of view is 120 × 120 arcsec.

calibration runs. These calibration images (along with flat field images taken during the day) are used in conjunction with the target images in the ESO software package. Telluric standards, observed through the night and with similar air mass and sky location as our cluster, were also extracted using the same methods as outlined above for the target objects. The telluric stars are also observed using an “ABBA” set, at similar locations on the array as the cluster to mitigate wavelength mismatches due to the warps in both the spectral and spatial direction on the array. We selected the telluric standard HD 174262, an A1 dwarf, because it was close in the sky to our targets and at a similar airmass. We also observed HD 171149, an A0 dwarf, for which a telluric free spectrum is available (Hanson et al. 2005). The later star was observed with a slightly higher airmass, but still could be used to effectively constrain the intrinsic hydrogen Brackett lines of HD 174262. With the hydrogen lines from HD 174262 modeled and removed, an excellent telluric spectrum was created to remove telluric contamination from our cluster stars using

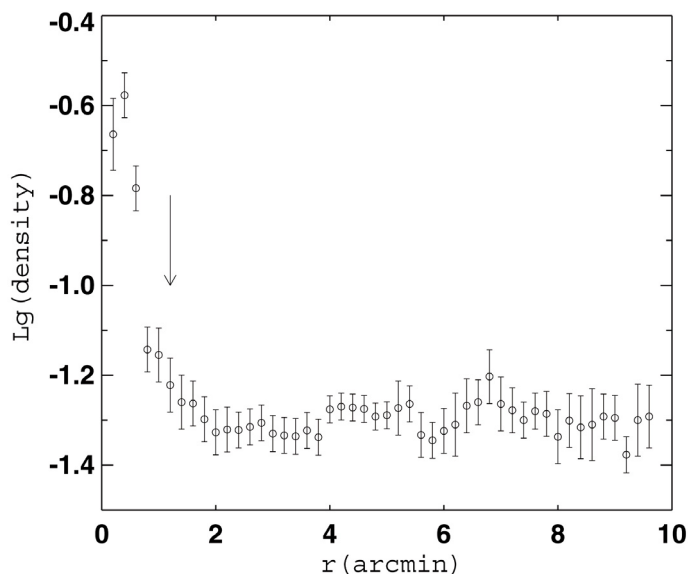


**Fig. 3.** Radial surface density (in number of stars per square arcsec) profile of Mercer 23. The bars show the  $3\sigma$  Poisson uncertainties. The arrow indicates the derived 1.2 arcmin cluster radius.

the cross-correlation IRAF routine, `telluric`, designed for this purpose.

The stars in our spectroscopic study ranged in magnitudes from 7th to greater than 14th. Because all the stars for the slit position containing Objects 9, 10 and 11 were relatively dim, we pushed the on-source integration times perhaps too far (400 s). The  $K$ -band spectrum looks very good, but we faced great difficulty fully removing the powerful OH lines in the  $H$ -band spectrum (the airmass was also quite high by then, at 2.0). Luckily, with the exception of the He I line at  $1.700 \mu\text{m}$ , and much of Object 9 ( $H = 13.0$ ) this did not greatly affect our ability to still provide a reasonable fit the broad stellar lines amongst the noisy, but sharp, residual peaks left after the OH subtraction.

### 3. $JHK_S$ color–magnitude and two-color diagrams

Mercer 23 suffers from heavy fore- and background stellar contamination, but it appears compact and stands out well above the surrounding field. Since we did not observe a comparison field to decontaminate the color–magnitude diagram we retrieved near-infrared photometry from the UKIDSS Galactic Plane Survey (Lawrence et al. 2007). We have used data from the UKIDSS DR3 data release. The calibration of both sets of photometry is based on 2MASS magnitudes and the comparison between stars in common shows only very small differences (within 0.05). To determine the Mercer 23 boundaries we performed direct star counting, assuming spherical symmetry. The projected star number density as a function of radius is shown in Fig. 3. The cluster boundary was determined as the radius at which the density profile exceeds twice the standard deviation of the surface density in the surrounding field. This yields a radius of 1.2 arcmin.

The UKIDSS color–magnitude diagram of 5 arcmin radius around the cluster center is shown in Fig. 4 (left, top panel), while the area with the extraction radius of 1.2 arcmin is shown in the right panel. We also calculated the stellar surface-density distributions (number of stars per arcmin<sup>2</sup>) using Bonato & Bica (2009) approach for a grid size of  $0.5 \times 0.5$  arcmin<sup>2</sup>, centered on the apparent cluster center (shown in the left panel of Fig. 5). The overdensity of the cluster is well visible.

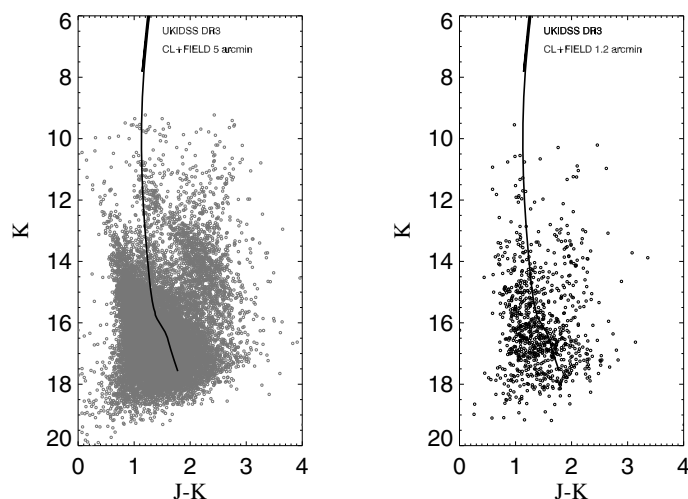


**Fig. 4.** Left panel: the UKIDSS ( $J - K, K$ ) color–magnitude diagram of the stars within a circle with radius  $R = 5$  arcmin around Mercer 23. Right panel shows the stars within radius  $R = 1.2$  arcmin. The solid line represents the 4 Myr isochrone taken from Padova’s library.

With the newly-adopted cluster radius, we statistically decontaminated our “cluster”+“field” color–magnitude diagram by removing as many stars as are present on the “field” color–magnitude diagram. The details of the procedure are described in Borissova et al. (2005) and Bonatto & Bica (2006). Basically, the decontamination algorithm divides the full range of magnitude and colors of a given CMD into 3D grids whose cubic cells have axes along the  $K_S, (J-H), (J-K_S)$  directions and computes the expected number-density of field stars in each cell based on the number of comparison field stars. The magnitude and colors of the field stars should be compatible with those of the cell. After that the expected number of field stars is randomly subtracted from each cell. We repeat the procedure 10 times, using different comparison fields taken from UKIDSS, located within  $R = 20\text{--}30$  arcmin. We have selected 362 potential cluster members. The most probable cluster members, plotted over the whole of the sample, is shown in the right panel of Fig. 5.

The decontaminated CMD (Fig. 6, right bottom panel) shows the typical sequence for a young open cluster: a well-developed MS detected down to  $\sim 15$  mag, and a rich population of PMS stars at  $14 < K_S < 19$  mag and  $2 < J-K_S < 2.5$  mag. To constrain the age and masses of these stars we applied isochrone fits with PMS tracks of different ages: 0.1, 1, 4, 7, and 10 Myr from Siess et al. (2000) shifted by the derived distance modulus and reddening to the cluster (see Sect. 5). Mindful of the photometric errors and crowding effects, we reach the tentative conclusion that the majority of the PMS candidates have ages between 1 and 10 Myr. A non-negligible number of objects fall to the right of the reddening vector for the reddest stars on the color-color diagram. Most likely they have an excess due to circumstellar material.

### 4. Spectral analysis of the targets

Spectroscopically observed candidate cluster members are identified in Fig. 2. Their coordinates and magnitudes are given in Table 2. The magnitudes of the brightest stars, saturated on PANIC images, are taken from 2MASS. The errors for both 2MASS and PANIC photometry are the combined (total) photometric uncertainties including PSF errors and zero points. The Obj1, noted with asterisk in this table, has very small angular

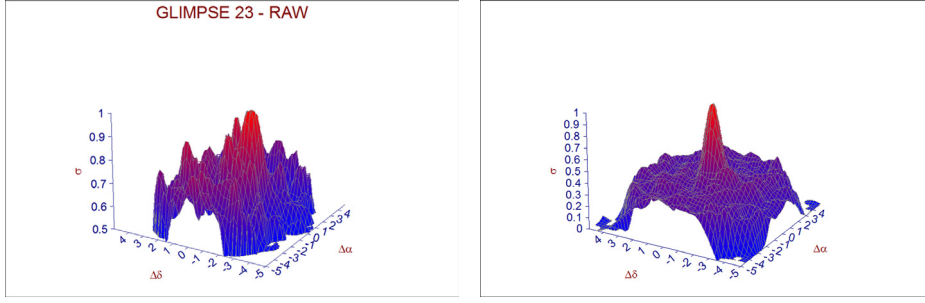


**Fig. 5.** The stellar surface-density distributions (number of stars per arcmin<sup>2</sup>) of Mercer 23. *Left panel:* all stars in 5 arcmin radius taken from UKIDSS. *Right panel:* most probable cluster members overplotted on the whole sample. The X and Y axes are in degrees. The stellar surface-density is normalized to 1.

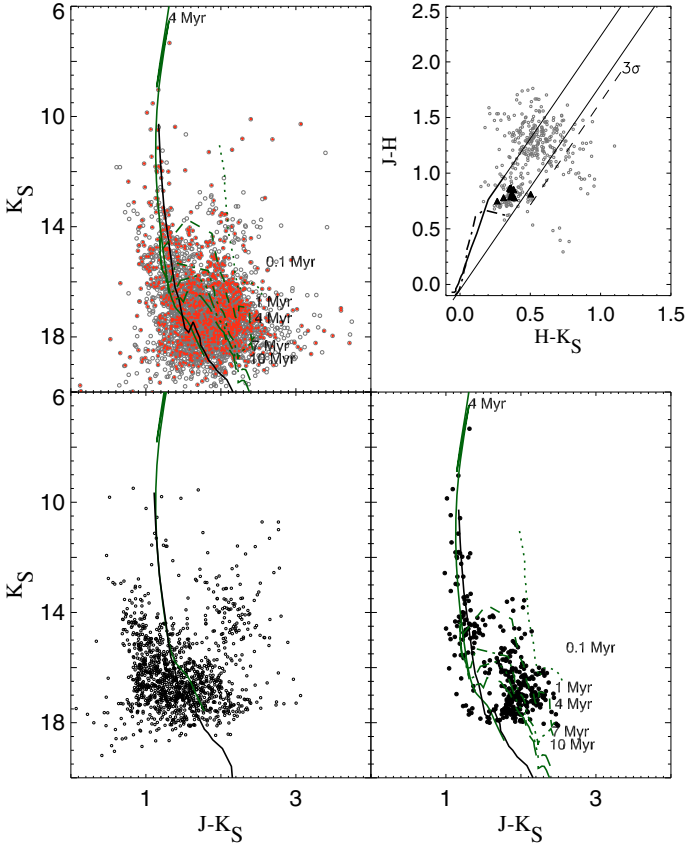


**Fig. 6.** *Top Left panel:*  $(J-K_S, K_S)$  color–magnitude diagram of the stars within a circle with radius  $R = 1.2$  arcsec around Mercer 23 (filled circles) overlotted on the whole sample of stars in our field of view (open circles). *Top Right panel:*  $H-K_S, J-H$  two-color diagram of the decontaminated CMD of the cluster. The triangles represent spectroscopically observed stars, the continuous and dotted lines represent the sequence of the zero-reddening stars of luminosity classes I (Koornneef 1983) and V (Schmidt-Kaler 1982), respectively. Reddening vectors for O5V and M5I stars are also shown. *Bottom left panel:* CMD of the typical UKIDSS comparison field. *Bottom right panel:* decontaminated CMD of Mercer 23. The 0.1 to 10 Myr PMS isochrones (dotted lines) are taken from Siess et al. (2000), while the 4 Myr isochrone (solid line) is taken from Padova’s library.

separation from Obj2 on the 2MASS images and its photometry in the 2MASS All-Sky Point Source Catalog is not reliable. In order to improve the data for this star we provided PSF photometry with a small PSF radius on the 2MASS images and used the neighboring stars to transfer the magnitudes in to the 2MASS photometric system. Figure 7 identifies the location of all spectroscopically observed stars on the decontaminated CMD.

Our eleven spectra fall into two classes: three of them exhibit one or more emission lines, and the rest have only

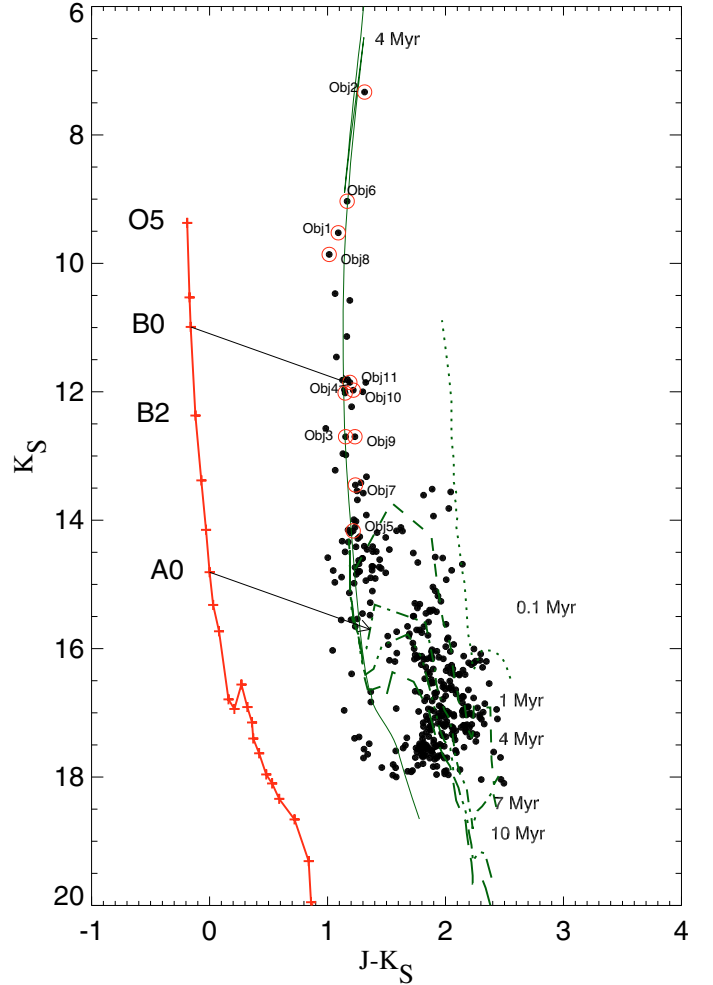


**Fig. 7.** The  $K_S$  versus  $(J-K_S)$  color–magnitude diagram of Mercer 23. The unreddened main sequence from Schmidt-Kaler (1982) is drawn with a heavy solid line. The adopted distance modulus is  $(m-M)_0 = 14.08$  mag. The stars with known spectral types are labeled. The light solid line of the main sequence and the PMS isochrones are reddened by 1.36 in  $E(J-K_S)$ . The 0.1, 1, 7 and 10 Myr PMS isochrones are taken from Siess et al. (2000), while the 4 Myr isochrone is taken from Girardi et al. (2002). Objects 1, 2 and 6 clearly show  $K$  magnitudes consistent with post-main sequence evolution, while the remaining stars are consistent with being main sequence late-O or early-B stars.

absorption features. We first determined their spectral classes from a direct comparison with template stellar spectra from the atlas of Hanson et al. (2005). The spectra from this atlas are taken with higher spectral resolution ( $R = 9000\text{--}12000$ ) and were rebinned to  $R = 4000$ . A further analysis was done based on cross-correlating the stellar spectra with a grid of OB star models. Finally, a full NLTE analysis was undertaken on the

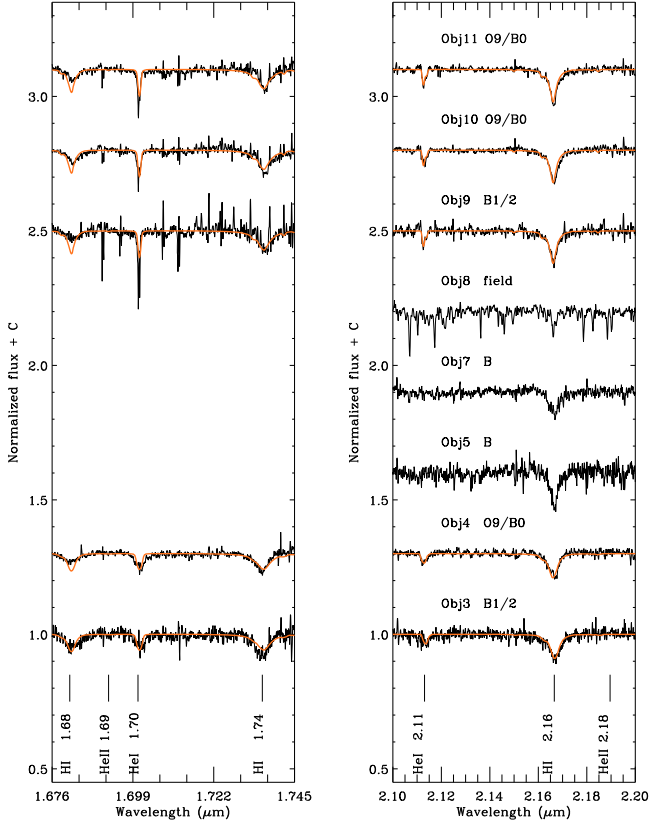


**Fig. 8.** The ISAAC spectra of the absorption line stars of Mercer 23. The different spectra have been arbitrarily shifted along the flux  $F_{\lambda}$  axis for clarity. The dashed lines indicate the rest-frame wavelengths of the spectral features. The adopted model spectra for Objs. 3, 4, 9, 10 and 11 are over plotted.

three most luminous stars to derive their full stellar properties (luminosity, wind, etc.).

#### 4.1. Spectral classification of the absorption line stars

The spectra of stars showing only absorption lines are shown in Fig. 8. These were taken with ISAAC ( $R \approx 4000$ ) and have signal to noise ratio at or well above 80. The only exception is Obj5, our dimmest object ( $K_S = 14.1$ ) with  $S/N = 60$  in its  $K$ -band spectrum. Obj3 was observed with two different slits in both bands, which allowed us to confirm the reliability of the reduction procedure, as well as the wavelength calibration, which is determined to be better than  $\pm 3 \text{ km s}^{-1}$ .

Objects 3, 4, 9, 10 and 11 show reasonably strong He I 2.112/3  $\mu\text{m}$  and Br $\gamma$ . Based on typical line ratios seen in other studies of late-O and early-B stars (Hanson et al. 1996; Bik et al. 2005) we would classify all of them as O9-B2 stars. In the spectra of the next brightest stars Object 5, and 7, the only visible feature is Br $\gamma$  in absorption. The strength of Br $\gamma$  alone is a notoriously weak indicator of spectral type (Bik et al. 2005). Rather spectral typing needs to be done as a comparison of two or more features. Because Obj5 and 7 have nothing but Br $\gamma$ , these stars can only be classified simply as B stars. As their Br $\gamma$  is not particularly strong, and based on their relative photometry, we expect them to be mid-B, B3/4 – certainly nothing later than B6, after which the Br $\gamma$  line will be seen to increase in strength significantly (Hanson et al. 1996). If all of these B stars are in the cluster, they are almost certainly dwarfs, but this is not based on

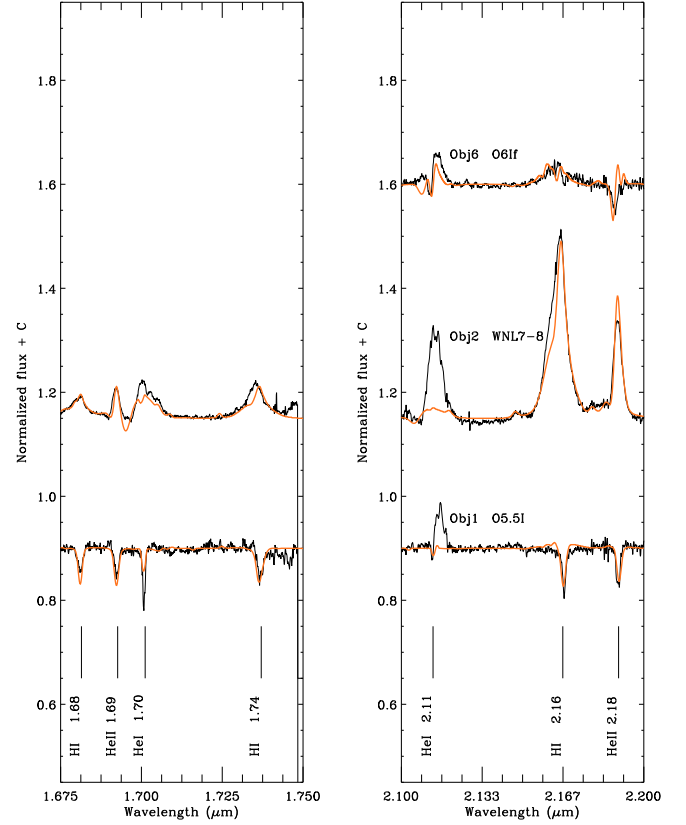


**Fig. 9.** The ISAAC spectra of the emission line stars of Mercer 23. The different spectra have been arbitrarily shifted along the flux  $F_{\lambda}$  axis for clarity. The dashed lines indicate the rest-frame wavelengths of the spectral features. The best models are overplotted. Our models do not include the emission transition seen at 2.155  $\mu\text{m}$ , due to C III/N III/O III blend.

the infrared spectra. This claim is based on their apparent luminosity, colors and the well fit isochrone of a young cluster. The existence of the three very luminous evolved stars (Sect. 4.2, below) also points to a young enough age that we would not expect these stars to have moved significantly from the zero-age main sequence. The final star from our sample for which we obtained spectra is Object 8. According to its  $K$ -band spectrum, Object 8 looks to be a non-member, showing numerous, narrow, metal lines typical of a cool field star.

We derived the radial velocities of the absorption line stars with the IRAF task `fxcor`. The four radial velocity standards are used HD 37468 (O9.5V); HD 36166 (B2V); HD 167785 (B2V) and HD 191639 (B1V). The first two radial velocity standards are taken from Hanson et al. (2005) spectral atlas, while the last two stars were observed by us. The radial velocities and their standard deviation errors are given in cols. 12 and 13 of Table 2. The weighted mean (some of the radial velocities are measured using only one line) is calculated as  $V_{\text{rad}} = 70 \pm 5 \text{ km s}^{-1}$ . The uncertainty is determined from Poisson statistics of the measurements and the error of the wavelength solution.

#### 4.2. Spectral classification of emission line stars

Three of our spectroscopic targets, Obj1, 2 and 6 and shown in Fig. 9, have emission lines in their spectra. Objects 1 and 6 both show the 2.112/3–2.155  $\mu\text{m}$  He I/N III complex. Br $\gamma$  is in narrow absorption in Obj1 and weak emission in Obj6. Both Obj1 and 6

**Table 3.** Physical parameters of spectroscopically analyzed stars in Mercer 23.

Star	Sp Typ	$\log L$ [ $L_{\odot}$ ]	$\dot{M}^a$ [ $M_{\odot}\text{yr}^{-1}$ ]	$T_{\text{eff}}$ [K]	$\log g$	$E(J-K_S)$	$(K_S-M_{K_S})_0$
Obj1	O5.5 I	6.21	$1.5 \times 10^{-5}$	35 000	3.25	1.30	14.20
Obj2	WNL7-8	6.56	$2.4 \times 10^{-5}$	38 000	3.00		
Obj3	B1/2	4.39		32 500	4.25	1.29	13.64
Obj4	O9/B0	4.65		32 500	4.25	1.32	14.55
Obj5	B3/4					1.38	14.49
Obj6	O6 If	5.86	$2.1 \times 10^{-5}$	34 000	3.25	1.38	13.67
Obj7	B3/4					1.35	13.84
Obj9	B1/2	4.33		30 000	4.25	1.37	13.59
Obj10	O9/B0	4.72		30 000	4.25	1.39	14.46
Obj11	O9/B0	4.64		30 000	4.25	1.36	14.36

**Notes.** <sup>(a)</sup> Only objects 1, 2 and 6 had a modeled wind component providing a mass loss rate. The value given in the table corresponds to a smooth wind. H/He ratio,  $\beta$  parameter, clumping factor ( $f$ ) and  $V_{\infty}$ , needed for the wind models and errors, are given in Sect. 4.4.

show He II 2.18  $\mu\text{m}$  in absorption. Finally, the H I Brackett lines of 1.67  $\mu\text{m}$ , and 1.74  $\mu\text{m}$ , He I 1.70  $\mu\text{m}$  and He II 1.69  $\mu\text{m}$  are all in absorption. While the  $K$ -band alone does not provide classifications as accurate as the optical, the early- and mid-O stars, by virtue of the very sensitive pairing of the He I 2.112/3 line with the N III complex at 2.155 provide the most accurate near-infrared spectral typing amongst OB stars (see Fig. 2 through 5 in Hanson et al. 2005). These set of features rather clearly indicate Obj1 to be O5–O6 based on the weak but significant He I 2.112. The fairly strong He I 1.700 is consistent with the star being later than O5 and looks quite a bit like the O5.5 I(f) star Cyg OB2 #8A in Hanson et al. (2005). The very luminous nature of Obj1 likewise indicates it is a supergiant, though not extreme enough to show Bry emission yet. The luminosity type is based solely on the apparent luminosity and assuming it a member of the cluster. The stronger He I 2.112/3 line in Obj6 suggests it is definitely later than O5, but with N III still stronger than He I, it is not so late as O7. We classify Obj6 as being an O6 and a definite supergiant based on the emission of Bry. Object 2 has all of its lines in the  $H$ - and  $K$ -band spectra in broad emission, consistent with a WR star. Bry is stronger than the 2.112/3–2.155  $\mu\text{m}$  He/N III complex and He II 2.189  $\mu\text{m}$  is weaker than Bry. These ratios lead to an approximate WN 7-8h spectral classification based on Crowther & Smith (1996).

#### 4.3. Using an OB model grid to derive stellar properties

The spectral classifications described above give a rough estimate of the temperature of our stars, but luminosity class is often unconstrained through pure morphological classification of the spectra. The precision of spectral classification is related to the intrinsic variation within the classes and the paucity of reliable luminosity indicators in the near-infrared. Moreover, the exact parameters of WR and O supergiant stars, even among similar optical spectral types, are not very homogeneous in luminosity. In order to better analyze the evolutionary status of our stars and how the most massive stars populate the cluster’s HR diagram we need more precise estimates of temperature and luminosity for each star.

The analysis of the 8 absorption line stars and the three emission line stars were performed in different ways. In order to obtain an estimate of the temperature and gravity of the absorption line stars we applied the method used for follow up studies on transiting planets (Latham 2003). We cross correlated our observed near-infrared spectra with a template

library and assign to the star the  $T_{\text{eff}}$  and  $\log g$  of the model with the highest value of the cross correlation function. As a template library we used our grid of O star models (kook-aburra.phyast.pitt.edu/hillier/web/CMFGEN.htm), which were based on the original O-star grid of Martins et al. (2005) and are located at [www.graal.univ-montp2.fr/hosted/martins/SED.html](http://www.graal.univ-montp2.fr/hosted/martins/SED.html).

The results of these analyses,  $T_{\text{eff}}$  and  $\log g$  for the five late-O/early-B stars where a reasonable conversion of the model was possible, are given in Table 3. The selected best models are overplotted on the observed spectra in Fig. 8. Note, the two cooler B stars, Obj5 and Obj7 have virtually no trace of He I and no  $H$ -band spectrum. A model for  $T_{\text{eff}}$  and  $\log g$  could not be constrained with the single Bry line for these stars. For the five absorption stars where an analysis was possible, their spectra are consistent with late-O or early-B dwarfs. Obj8 is also missing from the table, as it is not an early type star and thus a non-member of Mercer 23.

#### 4.4. Spectral quantitative analysis of the emission line stars

For the emission line stars we used models adjusted for each star. These models were also calculated by the CMFGEN code (Hillier & Miller 1998). The wind of the star was described by a pseudo hydrostatic structure connected to a standard  $\beta$  velocity law as described by Hillier et al. (2003). The absence of P Cyg features in the spectra limited the precision of  $V_{\infty}$ . We adopted 1500  $\text{km s}^{-1}$  for Obj2, 1000  $\text{km s}^{-1}$  for Obj6 and 2100  $\text{km s}^{-1}$  for Obj1. This values of  $V_{\infty}$  reproduced well the width of Bry in the two stars with this line in emission. The  $\beta$  parameter was set to 1.0 for Obj2 and to 0.8 for Obj1 and Obj6. These are the usual values obtained for WR and O stars, respectively. The winds of luminous, hot stars are believed to be clumpy (Moffat 2008). Again, the limited number of diagnostic lines did not allow for an independent determination of the clumping factor so we set it to the “standard” value  $f = 0.1$  (Moffat 2008; Hamann & Koesterke 1998; Crowther et al. 2002, 2006a,b).

Similar to Martins et al. (2008), we run these models with complex atoms including CNO, Si, P, S and Fe. All of these elements play an important role in the energy balance through the wind. The limited number of lines in the  $H$  and  $K$  atmospheric window prevent the detailed analysis of the chemical composition, but one does not expect a significant change in the abundances of the elements heavier than oxygen. Hence, we simplified the analysis by fixing the abundances of these elements to

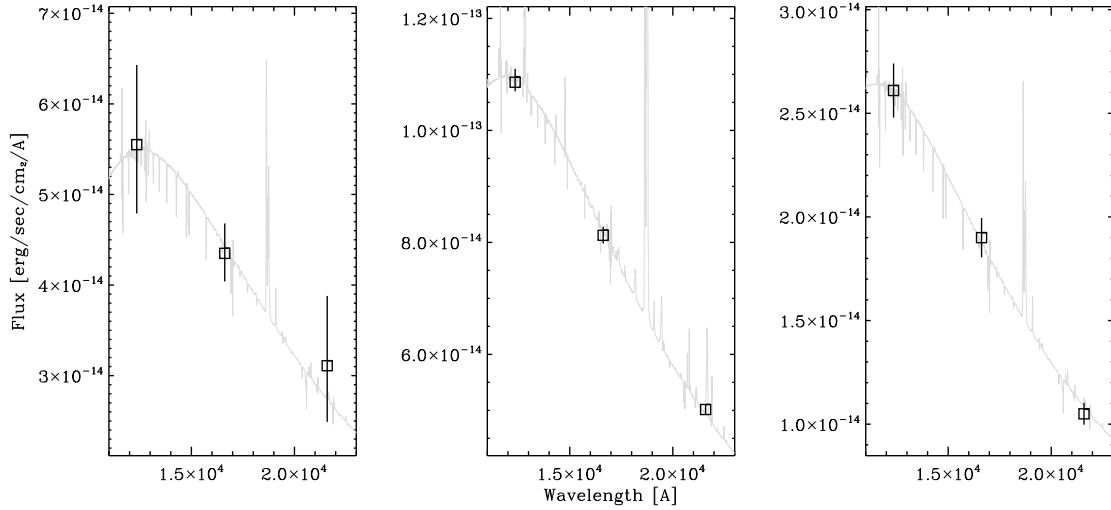


**Fig. 10.** Comparison between photometric fluxes (filled squares) and synthetic spectra (gray line) for the three brightest stars. *From left to right* they are: Obj1 (O5 I), Obj2 (WR star) and Obj6 (O6 I). The error bars corresponds to the photometric errors.

solar values. On the other hand, the abundances of CNO can be altered by the stellar evolution and their actual values need to be taken into account. Unfortunately, our VLT *K*-band spectra only cover the range from 2.09 to 2.25  $\mu\text{m}$  and miss the strategic C IV 2.070/2.084  $\mu\text{m}$  and N III 2.247, 2.251  $\mu\text{m}$  lines. This prevents us from determining the C and N composition directly. The other prominent feature in the *K* spectra is the He I/N III/O III/C III blend at 2.112/3–2.155  $\mu\text{m}$ . But the modeled emission of this blend depends not only on the temperature, gravity, mass loss rate and chemical composition but also on the atomic data and how they are treated in the code (Martins et al. 2008). This limits its use as a feature to diagnose abundances. We decided not to model this blend and we used solar CNO abundance for Obj1 and Obj6. However, the CNO abundance can not be set to solar for Obj2, the WR star, for which a significant change in abundances are to be expected. To address this problem, we compared our synthetic spectra with a previously published low resolution SofI spectra of Obj2 (Kurtev et al. 2009). This spectrum covers C IV 2.070/2.084  $\mu\text{m}$  and N III 2.247, 2.251  $\mu\text{m}$ . The low resolution and S/N of these SofI only allow us to estimate an upper limit of the abundances of C and N. For Obj2 we obtain a reduction of C abundance by 1/3 to 1/6 and an increase of N abundance by factor a 5 to 10 compared to solar.

Once the wind structure and atomic abundances were set, we used the ratio of the He I and He II lines as the temperature diagnostic and to constrain the He/H abundances. For Obj1, similar to the absorption line stars, we cross correlated the observed spectrum with the grid of models mentioned above to give us an initial guess for the temperature. The Brackett gamma and He II 2.18 lines of this star are very narrow. To fit their profiles we reduced the gravity to  $\log g = 3.0$ , which confirms the supergiant nature of this star. However, the temperature of this object posed a problem. Based on the *H*-band ratio He I 1.70/He II 1.69, gives a value of  $T_{\text{eff}} = 33\,000$  K, or about O7. On the other hand, the very weak *K*-band He I 2.12  $\mu\text{m}$  line, Br  $\gamma$  and strong He II 2.189 is consistent with something much hotter, 37 000 K or about O5.5. The discrepancy lies entirely with the surprisingly strong He I line at 1.70 which is not consistent with any of the remaining diagnostics. This line is often contaminated by atmospheric OH band (see Fig. 8). Unfortunately, the small number of diagnostic lines does not allow a solution to this problem. We

will assume the anomaly exists in the He I 1.700 line and assign a temperature of 35 000 K. We stress our purpose is to situate the emission line stars on the HR diagram, we can not always make a perfect model of their wind.

Obj2 and Obj6 posed no such difficulties in regards to their modeled temperature. Figure 9 shows the models which match the expected temperature of these stars based on their *K*-band spectral type. The modeled parameters are presented in Table 3. These two stars have spectra that look morphologically similar to F4 and F15 of Arches cluster (Martins et al. 2008). In both cases, our temperatures agree very well with the temperatures derived by Martins et al. (2008) for their F4 and F15 stars.

Once the temperature of the stars were determined, we compared the model fluxes to the ones obtained from our *JHK<sub>S</sub>* photometry and obtain the luminosity. First we converted the observed *J*, *H* and *K<sub>S</sub>* magnitudes to fluxes using the SPITZER Magnitude to Flux Density converter (<http://ssc.spitzer.caltech.edu/tools/magtojy>). Then the model fluxes were reddened with the Cardelli et al. (1989, CCM)  $R_V = 3.1$  reddening law. The  $E(B-V)$  and the luminosity were adjusted until the observed fluxes were reproduced by the models. The obtained luminosities and  $E(B-V)$  values are given in Table 3. The reddening obtained by this procedure is compatible with the one obtained from the photometry. The good agreement between the photometric fluxes, the derived reddening and the model fluxes (Fig. 10) provide confidence to the derived temperature and mass loss rates of the emission line stars.

Let us discuss the expected error in our quantitative analysis. The models we used have a roughly estimated terminal velocity  $V_\infty$  and an assumed velocity law,  $\beta$ . One must keep in mind the influence on the results if these parameters are changed. The intensity of the emission lines is determined by the transformed radius  $R_t$

$$R_t = R_{\text{star}} \left( \frac{V_\infty}{\dot{M}} \right)^{2/3}. \quad (1)$$

Models with the same  $R_t$  produce similar spectra (Schmutz et al. 1989), which means that the same synthetic spectrum will be obtained if the size of the star and the ratio of  $V_\infty/\dot{M}$  is maintained fixed. Therefore different value of  $V_\infty$  will lead to different  $\dot{M}$ . The observed values of  $V_\infty$  for WR stars is between 1000 and

3000 km s<sup>-1</sup>. So we can expect a change in  $V_\infty$  and therefore in  $\dot{M}$  less than a factor of 2. An increase in  $\dot{M}$  leads to a cooler wind and a small increase in the luminosity is usually needed to maintain the line ratios. But the changes in the temperature rarely are more than 1000 K for the expected changes in  $\dot{M}$ . A change of 1000 K in temperature for  $T \sim 35$  kK leads to  $\sim 0.05$  dex change in luminosity.

The effect of different values of  $\beta$  is more difficult to estimate, but roughly, a bigger value of  $\beta$  increases the density in the inner wind and might increase the intensity of the helium lines. Therefore, a different  $\beta$  may lead to a different value of He/H abundance and from there to a slightly different combination of  $T_{\text{eff}}$ ,  $\dot{M}$  and luminosity. The quantitative analysis of the errors is difficult. To account for all these effects, we assume errors of  $\pm 3000$  K in temperature, 0.2 dex in mass loss rate and luminosity (for a given distance) and 0.25 in  $\log g$  for all stars analyzed in this paper. Similar errors were used by Martins et al. (2008).

## 5. Physical parameters of the Mercer 23 stellar cluster

### 5.1. Reddening and distance towards the cluster

The location of the cluster stars in the color-color diagram,  $J-H$  vs.  $H-K_S$ , allows us to estimate their individual extinction values. In the case of Mercer 23 the cluster members occupy a relatively well-defined locus on the color-color diagram at  $H-K_S \sim 0.6-0.8$  mag and  $J-H \sim 1.0-1.3$  mag (see the triangles in Fig. 6, top right panel). First, we simply measured the color excesses of this locus on the color-color diagram with respect to the sequences of unreddened MS stars (Schmidt-Kaler 1982), obtaining  $E(J-K_S) = 1.39 \pm 0.06$  mag. Throughout this analysis we used the reddening law of Rieke & Lebofsky (1985, RH85). In the infrared bands and with this level of moderate extinction, this is the same as using CCM with a ratio of total to selective extinction,  $R_V = 3.1$ .

The reddening can also be determined from the apparent MS colors, given that the MS of young clusters is nearly vertical. Applying this method and fitting only unevolved cluster MS stars with the 4 Myr Geneva isochrone (Girardi et al. 2002) we obtained  $E(J-K_S) = 1.25 \pm 0.10$  mag.

And finally, we used the intrinsic  $J-K_S$  colors of OB stars (Schmidt-Kaler 1982; Koornneef 1983; Martins & Plez 2006) to calculate the individual color excesses of the spectroscopically-classified stars. They are given in the Table 3. The calculated mean value is  $E(J-K_S) = 1.36 \pm 0.02$  mag.

As a final reddening of the cluster we adopted a weighted mean value of the previous measures, giving  $E(J-K_S) = 1.35 \pm 0.05$  mag. Using RH85 and Hanson (2003) for the  $A_{K_S}/A_V$ , this equates to  $A_V = 7.2$  mag. This value is very close to that determined by Kronberger et al. (2006).

To determine the distance to the cluster, we used the  $K$ -band spectral classification of our O and B type objects and the intrinsic color and absolute magnitudes of the O type supergiants and the B type main sequence stars taken from Martins & Plez (2006) and Schmidt-Kaler (1982). We estimated the uncertainty of the classification to be 1 or 2 (in the worst cases) spectral subtypes. Similar errors are reported by Martins et al. (2008). The individual distances of the stars are given in the last column of the Table 3. The unweighted mean distance is  $(K_S - M_{K_S})_0 = 14.08 \pm 0.21$  mag. This corresponds to a distance of  $D = 6.5 \pm 0.3$  kpc. The errors are calculated taking into account Poisson statistics of the measurements, photometric errors

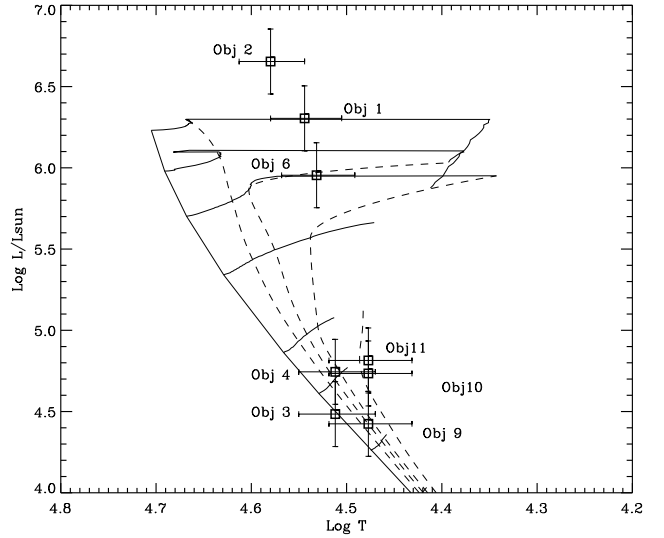


**Fig. 11.** The HR diagram for Mercer 23 based on the eight member stars with good quality  $H$ - and  $K$ -band spectra using Geneva (Meynet & Maeder 2003) evolutionary tracks with rotation (300 km s<sup>-1</sup> initial). The solid horizontal lines represent the mass tracks for stellar masses 120, 85, 60, 40, 25, 15 and 12  $M_\odot$ . The vertical solid lines represents a  $2 \times 10^6$  year stellar isochrone. The dashed lines represent stellar isochrones for cluster ages 3, 4 and  $6 \times 10^6$  years.

and the uncertainty of the spectral type determination. Following Davies et al. (2008) we calculated the tangential velocity in the direction of Mercer 23 of  $V_{\text{tan}} = 63 \pm 20$  km s<sup>-1</sup> and kinematic distance of 5.2 Kpc. Within the large uncertainties of this method we consider such obtained value as an acceptable agreement with our spectrophotometric distance.

### 5.2. Age of the cluster

Figure 11 shows the HR diagram of the 8 stars with modeled spectra in the cluster. We overplot the evolutionary tracks from Meynet & Maeder (2003). The isochrones at 2, 3, 4, and 6 Myr from the same tracks are overplotted also. The 5 absorption line stars, Obj3, 4, 9, 10 and 11, lie close to the main sequence. The isochrones in this region are barely separated and the errors in stellar temperatures and luminosities do not allow a reliable determination of the cluster age, though the stars are probably younger than 8 Myr. Obj6, on the other hand, lies between the 3 and 4 Myr isochrone and even though we assumed rather ample error bars, it cannot be older than about 4 Myr. The two brighter stars (Obj1 and Obj2) are younger than 3 Myr. As a result, the HR diagram of Mercer 23 shows a spread of ages between 2 and 4 Myr.

The age of the PMS stars was determined by fitting theoretical 0.1, 1.0, 4.0, 7.0, and 10 Myr PMS isochrones from Siess et al. (2000) to the CMD (Fig. 7). Note that the PMS stars spread over a wide age range but the main locus is between the 1 and 4 Myr isochrones. There are some stars with ages less than 1 Myr.

Additionally, the fraction of stars with NIR-excess correlates inversely with the stellar age over small age ranges (Hillenbrand 2005). The vast majority ( $\sim 90\%$ ) of stars older than 3–8 Myr cease to show evidence for a circumstellar disc, manifested in an excess of radiation in the  $K$ - and possibly  $H$ -band. The fraction of such low mass IR-excess stars in a very young stellar

**Table 4.** Mass of MS and PMS stellar content of Mercer 23.

Mag.Int. mag	Mass 4 Myr	$N_{MS}$	Mass 0.1 Myr	$N_{PMS}$	Mass 1 Myr	$N_{PMS}$	Mass 4 Myr	$N_{PMS}$	Mass 7 Myr	$N_{PMS}$	Mass 10 Myr	$N_{PMS}$	Total mass
-8	35.1	1	–	–	–	–	–	–	–	–	–	–	35
-7	33.0	2	–	–	–	–	–	–	–	–	–	–	66
-6	32.9	1	–	–	–	–	–	–	–	–	–	–	33
-5	28.8	2	–	–	–	–	–	–	–	–	–	–	58
-4	21.5	9	–	–	–	–	–	–	–	–	–	–	194
-3	14.0	9	–	–	–	–	–	–	–	–	–	–	126
-2	10.5	8	1.96	4	4	1	0	0	0	0	0	0	96
-1	6.0	44	1.20	2	4.9	7	6	0	6	0	6	0	301
0	3.8	29	0.51	1	1.98	11	2.98	15	2.85	6	3.75	0	192
1	1.9	7	0.21	11	0.83	31	1.75	20	2.21	21	2.09	7	138
2	1.0	0	0	0	0.35	25	1.1	21	1.3	12	1.3	55	119

cluster like Mercer 23 can be used as a crude age indicator. We determined that for Mercer 23 the fraction of low mass stars with photometry showing an IR-excess is 10%. The empirical calibration of Hillenbrand (2005) suggests a lower limit age of several million years for the low mass stars, in agreement with our previous estimations based on the high mass star properties.

### 5.3. Mass of Mercer 23

The decontaminated CMD shows a rather poorly populated main sequence (MS) and a significant presence of pre-main sequence (PMS) stars. To calculate the total mass of all our observed stars, we counted the number of MS stars for a given magnitude interval. The corresponding stellar mass in each magnitude bin is taken from the mass-luminosity relation derived from the isochrone fits described above. Summing the values in each magnitude bin produces the total number ( $N_{MS}$ ,  $N_{PMS}$ ) and mass of MS stars and PMS, respectively. The are given in Table 4.

In summary, the total number of observed cluster members is 362, from which 112 are main sequence stars and 250 are pre-main sequence stars. They give respectively a total mass of MS stars  $981 M_{\odot}$  and PMS stars contain  $376 M_{\odot}$ . The total mass of all observed cluster members is thus  $\sim 1360 M_{\odot}$ . Integrating over 2 Myr isochrone gives for the same mass interval  $\sim 1455 M_{\odot}$ . Since no completeness correction has been applied this value should be treated as a lower mass limit of the cluster. The total cluster mass, depending on the exact shape of the mass function at the low mass end, is likely a few times this value, or  $3\text{--}5 \times 10^3 M_{\odot}$ . Is this consistent with Mercer 23's three, very massive stars? Each has a mass at least as high as  $\Theta^1$  Ori C, the dominate O6 dwarf star located in the Orion Trapezium cluster with an estimated cluster mass of  $\sim 2 \times 10^3 M_{\odot}$  (Hillenbrand 1997). The Mercer 23 cluster might be compared to a younger and slightly more massive version of one of the Perseus twin clusters, h or  $\chi$ , each with masses of from  $\sim 4\text{--}6 \times 10^3 M_{\odot}$  (Bragg & Kenyon 2005). Another possibility is that we've underestimated the mass contribution of the unseen stars in the cluster.

## 6. Conclusions

We report new results of our long term project to study obscured Milky Way star clusters. We obtained deep *JHK<sub>s</sub>* imaging and *H*- and *K*-band spectroscopy of Mercer 23, a dense stellar cluster with one spectroscopically confirmed WR star and a sizable population of young stellar objects. The cluster is located at a distance of 6.5 kpc from the Sun. We have used numerous

indicators to establish that the cluster is very young, 2–4 Myr based on both it's high and low mass stellar population.

The formation and early evolution of the most massive stars are poorly unknown. This period of the star's life is very short and there are only a handful of objects observed in that particular stage. For this reason, the three most massive members of Mercer 23 deserved special attention. To this end, we've completed a spectral analysis and modeling of the *H*- and *K*-band spectra for these three, very massive post-main sequence objects.

Object 2 is a hydrogen rich WN7-8 star with progenitor mass well above  $80 M_{\odot}$ . Its temperature and very high luminosity is similar to the WR/LBV system HD 5980 in SMC (Foellmi et al. 2008). HD 5980 is the only known WR star with LBV like variability. Obj2 might be another example of a WR/LBV star. It could be connected with the nearby X-ray source 2E 1928.0+1825 = 2RXP J193013.8+183216 reported in Harris et al. (1994). It will be important that Obj2 is monitored with future observations. The two remaining O supergiants, have lower, but similarly high masses ( $>60 M_{\odot}$ ). The distance (6.5 kpc) and galactic location ( $l = 54$ ) of Mercer 23 puts it inside the inner first quadrant of the galaxy where only a few massive clusters have thus far been found. Mercer 23 is yet another new member of the family of relatively massive young Galactic clusters being uncovered with recent infrared surveys.

*Acknowledgements.* The data used in this paper have been obtained with SofI/NTT and with ISAAC/VLT at the ESO La Silla and Paranal Observatories. We have used data from the UKIDSS Galactic Plane Survey (Lawrence et al. 2007) DR3 data release. UKIDSS uses the UKIRT Wide Field Camera (WFCAM; Casali et al. 2007). The photometric system is described in Hewett et al. (2006), and the calibration is described in Hodgkin et al. (2009). The pipeline processing and science archive are described in Irwin et al. (in prep) and Hambly et al. (2008). This publication makes use of data products from the Two Micron All Sky Survey, which is a joint project of the University of Massachusetts and the Infrared Processing and Analysis Center/California Institute of Technology, funded by the National Aeronautics and Space Administration and the National Science Foundation. This research has made use of the SIMBAD database, operated at CDS, Strasbourg, France. M.M.H. is grateful for the support provided her by the ESO Visiting Scientist Programme during an extended stay in late 2008 when the VLT spectra were reduced. M.M.H. acknowledges support for this work by the National Science Foundation under contract No. 0607497 to the University of Cincinnati. J.B. acknowledges support from FONDECYT Regular #1080086 and MIDEPLAN ICM Nucleus P07-021-F. LNG is thankful for the support from Mexican CONACyT project 83016 and UNAM/PAPIIT IN123309. R.K. acknowledges support from Proyecto FONDECYT Regular #1080154 and Centro de Astrofísica de Valparaíso. D.M. is supported by grants from FONDAP CFA 15010003, BASAL CATA PFB-06, and MIDEPLAN MWM P07-021-F. We thanks the anonymous referee for the useful comments and suggestions.

## References

- Benjamin, R. A., Churchwell, E., et al. 2003, *PASP*, 115, 953
- Bica, E., Dutra, C. M., Soares, J., & Barbuy, B. 2003, *A&A*, 404, 223
- Bik, A., Kaper, L., Hanson, M. M., & Smits, M. 2005, *A&A*, 440, 121
- Bragg, A. E., & Kenyon, S. J. 2005, *ApJ*, 130, 134
- Boutloukos, S. G., & Lamers, H. J. G. L. M. 2003, *MNRAS*, 338, 717
- Bonatto, C., & Bica, E. 2006, *A&A*, 460, 83
- Bonatto, C., & Bica, E. 2009, *MNRAS*, 397, 1915
- Borissova, J., Pessev, P., Ivanov, V. D. et al. 2003, *A&A*, 411, 83
- Borissova, J., Ivanov, V. D., Minniti, D. et al. 2005, *A&A*, 435, 95
- Borissova, J., Ivanov, V. D., Minniti, D., & Geisler, D. 2006, *A&A*, 455, 923
- Borissova, J., Ivanov, V. D., Hanson, M. M., et al. 2008, *A&A*, 488, 151
- Cardelli, J., Clayton, G., & Mathis, J. 1989, *ApJ*, 345, 245
- Casali, M., Adamson, A., Alves de Oliveira, C., Almaini, O., & Burch, K. 2007, *A&A*, 467, 777
- Clark, J. S., Negueruela, I., Crowther, P. A., & Goodwin, S. P. 2005, *A&A*, 434, 949
- Crowther, P. A., Dessart, L., Hillier, D. J., Abbott, J. B., & Fullerton, A. W. 2002, *A&A*, 392, 653
- Crowther, P., & Smith, L. 1996, *A&A*, 305, 541
- Crowther, P. A., Morris, P. W., & Smith, J. D. 2006a, *ApJ*, 636, 1033
- Crowther, P., Hadfield, L., Clark, J., Negueruela, I., & Vacca, W. 2006b, *MNRAS*, 372, 1407
- Crowther, P. A., Smith, L. J., Hillier, D. J., & Schmutz, W. 1995, *A&A*, 293, 427
- Devillard, N. 2001, in *Astronomical Data Analysis Software and Systems X*, ed. F. R. Harnden, Jr., F. A. Brimini, & H. E. Payne, ASP Conf. Ser., 238, 525
- Davies, B., Figer, D., Law, C., Kudritzki, et al. 2008, *ApJ*, 676, 1016
- Dutra, C. M., & Bica, E. 2000, *A&A*, 359, 9
- Dutra, C. M., Bica, E., Soares, J., & Barbuy, B. 2003, *A&A*, 400, 533
- Figer, D. F., MacKenty, J. W., Robberto, M., et al. 2006, *ApJ*, 643, 1166
- Foellmi, C., et al. 2008, *Rev. Mex. Astron. Astrofis.*, 44, 3
- Froeblich, D., Scholz, A., & Raftery, C. L. 2007, *MNRAS*, 374, 399
- Gieles, M. 2009, *MNRAS*, 394, 2113
- Gieles, M., Larsen, S. S., Bastian, N., & Stein, I. T. 2006, *A&A*, 450, 129
- Girardi, L., Bertelli, G., Bressan, A., et al. 2002, *A&A*, 391, 195
- Hamann, W.-R., & Koesterke, L. 1998, *A&A*, 335, 1003
- Hamann, W.-R., Gräfener, G., & Liermann, A. 2006, *A&A*, 457, 1015
- Hambly, N. C., Collins, R. S., Cross, N. J. G., Mann, R. G., & Read, M. A. 2008, *MNRAS*, 384, 637
- Hanson, M. M. 2003, *ApJ*, 597, 957
- Hanson, M. M., & Bubnick, B. F. 2008, *PASP*, 120, 150
- Hanson, M. M., Conti, P. S., & Rieke, M. J. 1996, *ApJS*, 107, 281
- Hanson, M. M., Kudritzki, R.-P., Kenworthy, M. A., Puls, J., & Tokunaga, A. T. 2005, *ApJS*, 161, 154
- Harris, D. E., Forman, W., Gioia, I. M., et al. 1994, *EINSTEIN Observatory catalog of IPC X-ray sources*
- Hewett, P. C., Warren, S. J., Leggett, S. K., & Hodgkin, S. T. 2006, *MNRAS*, 367, 454
- Hillenbrand, L. 1997, *AJ*, 113, 1733
- Hillenbrand, L. 2005, Review article to appear in *A Decade of Discovery: Planets Around Other Stars*, STScI Symposium Series 19, ed. M. Livio [arXiv:astro-ph/0511083]
- Hillier, D. J., & Miller, D. L. 1998, *ApJ*, 496, 407
- Hillier, D. J., Lanz, T., Heap, S. R., et al. 2003, *ApJ*, 588, 1039
- Hodgkin, S. T., Irwin, M. J., Hewett, P. C., & Warren, S. J. 2009, *MNRAS*, 394, 675
- Holtzman, J. A., Faber, S. M., Shaya, E. J., et al. 1992, *AJ*, 103, 691
- Ivanov, V. D., Borissova, J., Pessev, P., et al. 2002, *A&A*, 349, 1
- Ivanov, V. D., Kurtev, R., & Borissova, J. 2005, *A&A*, 442, 195
- Koornneef, J. 1983, *A&A*, 128, 84
- Kronberger, M., Teutsch, P., Alessi, B., et al. 2006, *A&A*, 447, 921-928
- Kurtev, R., Borissova, J., Georgiev, L., Ortolani, S., & Ivanov, V. D. 2007, *A&A*, 475, 209
- Kurtev, R., Ivanov, V. D., Borissova, J., & Ortolani, S. 2008, *A&A*, 2008, 489, 586
- Kurtev, R., Borissova, J., Ivanov, V. D., & Georgiev, L. 2009, *Rev. Mex. Astron. Astrofis. Conf. Ser.*, 35, 160
- Lada, C. J., Lada, E. A. 2003, *ARA&A*, 41, 57
- Lamers, H. J. G. L. M. 2009, *Ap&SS*, 324, 183
- Lamers, H. J. G. L. M., Gieles, M., Bastian, N., et al. 2005, *A&A*, 117, 129
- Larsen, S. S. 2006, in *Proc. Globular Cluster – Guides to Galaxies*, ed. T. Richter, & S. S. Larsen [arXiv:astro-ph/0606625]
- Latham, D. W. 2003, *Scientific Frontiers in Research on Extrasolar Planets*, 294, 409
- Lawrence, A., Warren, S. J., Almaini, O., Edge, A. C., & Hambly, N. C. 2007, *MNRAS*, 379, 1955
- Maiolino, R., Rieke, G., & Rieke, M. 1996, *AJ*, 111, 537
- Martins, F., & Plez, B. 2006, *A&A*, 457, 637
- Martini, P., Persson, S. E., Murphy, D. C., et al. 2004, *Proc. SPIE*, 5492, 1653
- Martins, F., Schaerer, D., & Hillier, D. J. 2005, *A&A*, 436, 1049
- Martins, F., Hillier, D., Paumard, et al. 2008, *A&A*, 478, 219
- Mercer, E., Clemens, D., Meade, M., et al. 2005, *ApJ*, 635, 560
- Meynet, G., & Maeder, A. 2003, *A&A*, 404, 975
- Meynet, G., & Maeder, A. 2005, *A&A*, 429, 581
- Minniti, D., Lucas, P. W., Emerson, J. P., et al. 2010, *New Astron.*, 15, 433
- Moffat, A. F. J. 2008 in *Clumping in hot-star winds*, Proceedings of an international workshop held in Potsdam, Germany, 18–22 June 2007, ed. W.-R. Hamann, A. Feldmeier, L. M. Oskinova, 17
- Moorwood, A., Cuby, J. G., & Lidman, C. 1998, *The Messenger* 91, 9
- Rieke, G., & Lebofsky, M. 1985, *ApJ*, 288, 618
- Schmidt-Kaler, T. 1982, in *Landolt-Borstein, New Series, Group VI*, ed. K. Schaifers & H. H. Voigt (Berlin: Springer-Verlag), 2, 1
- Schmutz, W., Hamann, W.-R., & Wessolowski, U. 1989, *A&A*, 210, 236
- Siess, L., Dufour, E., & Forestini, M. 2000, *A&A*, 358, 593
- Skrutskie, M., Cutri, R. M., Stiening, R., et al. 2006, *AJ*, 131, 1163
- Vanbeveren, D. 2009, *New Astron. Rev.*, 53, 27
- Weidner, C., Kroupa, P., & Bonnell, I. A. D. 2009, *MNRAS*, 1552